Chapter 2

Theory of layered photonic structures

Qualitative and quantitative predictions of the diffraction of dielectric structures are instrumental for the interpretation of the experimental results collected in this study and reported in chapter 4. For this reason, the computation of the diffraction efficiencies of linear and periodic dielectric media is central to the present investigation.

In chapter 1 several modelling techniques have been mentioned, and the related issues and limitations in obtaining accurate predictions of the optical properties of periodic dielectric media have been briefly discussed. Some of those computational methods have been used in this study of the mechanisms of colour production on the wings of the tropical butterfly *Morpho rhetenor*. The choice of methods and their theoretical foundations are discussed here. The aim of this chapter is to provide the reader with the background necessary to support the theoretical and experimental investigations presented in later chapters, and the views presented therein.

First, the laws governing the propagation of electromagnetic waves in periodic media will be formalized for general models and arrangements. The symmetry of the systems successively considered permits use of low dimensional models and therefore the laws are expressed in their two-dimensional form and the consequences on the physics involved are discussed. While the general theory of electrodynamics in periodic media is nowadays firmly established, its application for modelling purposes is often specific to the structures investigated and the subject of constant research. The aspects of the general theory treated in this chapter are instrumental to the validation of the original modelling work presented thereafter.

Successively, with calculations performed using the previously introduced methods, an investigation of the photonic band structure of two *Bravais* lattices [88] is presented: a rectangular and a centred rectangular lattice. Both arrangements are important constituents of the microstructure occurring on the wings of the butterfly and no known investigation of these structures has been reported yet. A novel approach to calculating band diagrams over the complete *Brillouin* zone of the reciprocal periodic lattice has been produced for this study.

Finally, the theory of diffraction and field transformations is outlined in connection with the numerical methods used in the computation of the diffraction of periodic dielectric structures reported in chapter 5. The theoretical background of these methods are discussed in detail in the last sections of the chapter.

2.1 *Maxwell*'s equations in periodic media

The fundamental theory of the interaction of light and matter, or electromagnetic fields and charges, correct down to the atomic scale is called *quantum electrodynamics* and describes all processes of a world characterised by discrete energies, where forces are mediated by massless particles, the *photons.* However, when the number of charges and photons considered is large, their collective behaviour makes the detailed description of a quantum theory unnecessary and a classical representation of their dynamics becomes sufficiently accurate. The interaction between charges in macroscopic media is described via the classic electromagnetic vector fields, namely the electric field $\vec{E}(\vec{r})$, the magnetic field $\vec{H}(\vec{r})$, the dielectric displacement $\vec{D}(\vec{r})$ and the magnetic induction $\vec{B}(\vec{r})$, where the variable $\vec{r}$ denotes the position vector of the *Euclidean* space. The dynamics of these fields is governed by the following experimentally determined laws [89]: *Coulomb*'s law, *Faraday*'s induction law, the law describing the non-existence of isolated magnetic poles, and *Ampère*'s law. These laws are written in the SI system of units as follows:

$$\begin{aligned}
\int_{\partial V} \vec{D}(\vec{r}) \cdot \hat{n} da &= \int_V \rho(\vec{r}) dV, \\
\int_{\partial S} \vec{E}(\vec{r}) \cdot d\vec{l} &= -\frac{d}{dt} \int_S \vec{B}(\vec{r}) \cdot \hat{n} da, \\
\int_{\partial V} \vec{B}(\vec{r}) \cdot \hat{n} da &= 0, \\
\int_{\partial S} \vec{B}(\vec{r}) \cdot d\vec{l} &= \int_S \vec{j}(\vec{r}) \cdot \hat{n} da.
\end{aligned}$$

Integration in the above equations is indicated by the symbol dV when performed over a volume V, by da when over a surface S or over the surface ∂V of a volume V, and along the edge of a surface ∂S by $d\vec{l}$. The unit outward normal to the surface of integration is denoted by $\hat{n}$. The density of charges and the electric charge current is indicated by ρ and $\vec{j}$, respectively.

If the physical properties of the media are continuous these equations can be written as partial differential equations and are referred to as *Maxwell*'s equations [32]. In a non-magnetic, charge- and current-free ($\rho = 0$, $\vec{j} = 0$) medium they are as follows:

$$\begin{aligned} \nabla \cdot \vec{H}(\vec{r},t) = 0, \quad \nabla \times \vec{H}(\vec{r},t) &= \varepsilon(\vec{r})\epsilon_0 \frac{\partial \vec{E}}{\partial t}(\vec{r},t), \\ \nabla \cdot \varepsilon(\vec{r})\epsilon_0 \vec{E}(\vec{r},t) = 0, \quad \nabla \times \vec{E}(\vec{r},t) &= -\mu_0 \frac{\partial \vec{H}}{\partial t}(\vec{r},t), \end{aligned}$$

where the variable t indicates time, ϵ_0 and μ_0 are the permittivity and permeability of vacuum, while $\varepsilon(\vec{r})$ is the dielectric function of the medium. When the dielectric function is not continuous, *i.e.* in the presence of an interface, these equations alone are not valid anymore, but it can be proved that by making $\varepsilon(\vec{r})$ very fast changing and continuous, *Maxwell*'s equations imply that the tangential components of the electric and magnetic fields are continuous across an interface for current-free media [32, 89]. These boundary conditions ensure that the energy is conserved across the interface, which for continuous media is implicitly taken care of by the equations, and they are sufficient for a correct description of the propagation of electromagnetic waves where boundaries occur. In conclusion, the electromagnetic fields can be calculated in the presence of discontinuous media using *Maxwell*'s equations together with the above mentioned conditions of continuity of the fields.

The *Fourier* transform is a fundamental analytical tool in optics, which enables one to represent waves or arbitrary signals in the domain of their variables (be it time or position in space) or in the domain of their reciprocals. For example, transforming the fields from the time to the frequency domain allows one to analyse the spectral content of an optical signal or to express equations in a way that makes finding a solution simpler.

If we *Fourier*-transform *Maxwell*'s equations with respect to time t, we obtain:

$$\begin{aligned} \nabla \cdot \vec{H}(\vec{r},\omega) = 0, \quad \nabla \times \vec{H}(\vec{r},\omega) &= -i\omega\varepsilon(\vec{r})\epsilon_0 \vec{E}(\vec{r},\omega), \\ \nabla \cdot \varepsilon(\vec{r})\epsilon_0 \vec{E}(\vec{r},\omega) = 0, \quad \nabla \times \vec{E}(\vec{r},\omega) &= i\omega\mu_0 \vec{H}(\vec{r},\omega), \end{aligned}$$

where the angular frequency ω has substituted time as a variable of the fields. Concatenation of the inhomogeneous equations yields the following eigenvalue problem for the magnetic field in the space-frequency domain:

$$\nabla \times \left(\frac{1}{\varepsilon(\vec{r})} \nabla \times \vec{H}(\vec{r}, \omega) \right) = \frac{\omega^2}{\mathrm{c}^2} \vec{H}(\vec{r}, \omega), \tag{2.1}$$

where $\mathrm{c} = 1/\sqrt{\varepsilon_0 \mu_0}$ is the speed of light in vacuum. An analogous equation can be obtained for the electric field $\vec{E}$.

The operator $\Theta = \nabla \times (\varepsilon(\vec{r})^{-1} \nabla \times \bullet)$ of equation (2.1) is linear, and *Hermitian* with the *Euclidean* scalar product $(\vec{F}, \vec{G}) = \int \vec{F} \cdot \vec{G}^* dV$ if the integral is determined. Periodic systems or problems in which decay of the fields at large distances can be assumed, satisfy these requirements. These properties of the operator mean that it has real eigenvalues ω_p and its eigenvectors are orthogonal. It must be remembered that the eigenvectors $\vec{H}(\vec{r}, \omega)$ have to fulfil the condition of continuity of their tangential components wherever a boundary between two materials of different dielectric constant occurs, therefore the chosen solution formulation must satisfy this same condition.

It is interesting moreover to consider the mathematical relation between the symmetry of a problem and its solutions. A geometric operator S is called a *symmetry* of the operator Θ, and therefore of the problem, if both operators commute. It follows that they share the same eigenvectors. Some insight in the physics of the problem can then be gained from the study of its symmetries, as in the following examples:

- If $\varepsilon(\vec{r}) = \varepsilon(-\vec{r})$, which means that Θ is symmetric with respect to the inversion operation at the origin of the system of coordinates, then the solutions are either odd or even, because the eigenvalues of the symmetry are -1 and 1.

- If Θ is symmetric with respect to continuous translation in a plane, say xy, *i.e.* the problem is one-dimensional, the eigenvectors can have the form $\vec{H} = e^{ik_y y} \phi(z) \hat{x}$, which is a wave propagating in y direction ($\phi(z)$ is a scalar function, k_y the wave vector component in y direction, and $\hat{x}$ indicates the unit vector along the x direction). When this solution formulation is substituted in equation 2.1 one obtains

$$\frac{\partial^2 \phi}{\partial z^2} = \left(k_y^2 - \varepsilon(z) \frac{\omega^2}{\mathrm{c}^2} \right) \phi.$$

The solutions to the above equation have the form $\phi = Ae^{\alpha z}$, with A a scalar constant and $\alpha^2 = k_y^2 - \varepsilon \omega^2 / \mathrm{c}^2$. This corresponds to real, oscillating solutions above the light-line and complex, exponentially decaying (evanescent) ones below. Therefore, oscillating solutions exist in a material of higher index of refraction that cannot propagate in a lower index one, which explains total reflection at interfaces and confinement of guided modes in waveguides.

- For a periodic dielectric constant, say $\varepsilon(\vec{r} + \vec{R}) = \varepsilon(\vec{r})$ with $\vec{R} = pa\hat{x}$, a a constant and p any integer number, the operator Θ is symmetric with respect to the following discrete translation $T_{\vec{R}} \left(\vec{F}(\vec{r}) \right) = \vec{F}(\vec{r} + \vec{R})$, with $\vec{F}(\vec{r})$ any vector field. Consequently the eigenvectors of Θ are periodic. $T_{\vec{R}}$ has degenerate sets of eigenvectors $e^{i(k_x + qb)x}$ with $b = 2\pi/a$ and q any integer to eigenvalues $e^{ik_x pa}$. It follows that we can write the eigenvectors of Θ as

$$\begin{aligned} \vec{H}_{k_x}(\vec{r}) &= \sum_q \vec{c}_{k_x,q} e^{i(k_x + qb)x} \\ &= e^{ik_x x} \sum_q \vec{c}_{k_x,q} e^{iqbx} \\ &= e^{ik_x x} \vec{u}_{k_x}(x), \end{aligned}$$

  and $\vec{u}_{k_x}(x + pa) = \vec{u}_{k_x}(x)$, which is called a *Bloch* state [90].

The latter example corresponds to a *Fourier* expansion of the field, whereby the field is projected on a basis of continuous plane wave functions and is consequently continuous. This construction implicitly satisfies the condition of continuity of the field components tangential to interfaces in the solution of equation 2.1.

2.1.1 Two-dimensional problems: the ***Helmholtz*** equation

For a two-dimensional periodic arrangement, *Maxwell*'s equations reduce to scalar equations for specific choices of the field polarisation. Let the plane of the two-dimensional representation be xz. For a *transverse electric* (TE) polarised field, *i.e.* for an electric field oriented normally to the xz plane (in y direction) and having a vacuum wave number k_0, its magnitude obeys the following equation:

$$\left(\frac{\partial^2}{\partial x^2} + \frac{\partial^2}{\partial z^2} + k_0^2 \varepsilon(\vec{r})\right) E(\vec{r}) = 0, \tag{2.2}$$

which is called *Helmholtz* or wave equation. The magnitude of a *transverse magnetic* (TM) polarised field, *i.e.* a magnetic field oriented in y direction, obeys instead the following equation:

$$\left(\varepsilon(\vec{r})\left(\frac{\partial}{\partial x}\varepsilon(\vec{r})^{-1}\frac{\partial}{\partial x} + \frac{\partial}{\partial z}\varepsilon(\vec{r})^{-1}\frac{\partial}{\partial z}\right) + \frac{\partial^2}{\partial x^2} + \frac{\partial^2}{\partial z^2} + k_0^2 \varepsilon(\vec{r})\right) H(\vec{r}) = 0.$$

This equation reduces to the form of equation 2.2 for a dielectric function which does not vary in space.

It is apparent from these independent equations for the scalar field amplitudes that in a two-dimensional system the two orthogonal polarisations (TE and TM) are uncoupled. An arbitrary field can be decomposed in the two polarisations and these components can be propagated independently. This does not apply to three-dimensional problems, as for example for crystal lattices. In this case, the components of the vectorial *Maxwell*'s equations are coupled and cannot be solved separately, which results in the birefringence of three-dimensional PCs and the polarisation mixing of waves propagating in them.

2.1.2 Propagation in periodic media

In the eigenvalue problem arising from the concatenation of the inhomogeneous *Maxwell*'s equations, *i.e.* in equations 2.1 and 2.2, the dielectric constant or its inverse exerts a coupling between the space harmonics of the field within the periodic arrangement. This is best shown considering a one-dimensional periodic arrangement and waves propagating along its optical axis. The dielectric constant is periodic, therefore it can be *Fourier* expanded projecting it on the space harmonics of the lattice, just as the field eigenvectors, which decompose into *Bloch* states. The expansions of the dielectric constant $\varepsilon(\vec{r})$ and of the electric field $E(\vec{r})$ can be written as follows:

$$\begin{array}{ll} \varepsilon(\vec{r}) = \sum_p \varepsilon_p e^{ipbx}, & \varepsilon_p = (\varepsilon, e^{ipbx}), \\ E(\vec{r}) = \sum_q E_q e^{iqbx}, & E_q = (E, e^{iqbx}). \end{array}$$

where (ψ, ϕ) is the *Euclidean* scalar product, ε_p and E_p are the *Fourier* coefficients of the dielectric constant and electric field respectively, p and q are integer numbers, and b is the magnitude of the reciprocal lattice vector. Substitution of these forms in equation 2.2 yields a set of coupled equations,

$$k_0^2 E_q - b^2 \sum_p q(p+q)\varepsilon_{p-q} E_p = 0.$$

Here again k_0 is the vacuum wave number of the harmonic wave. The coupling between the *Fourier*-components of the field depends on the coefficients of the dielectric constant ε_{p-q}. After truncation of the sums, this set of equations can be written in the form of a matrix, which for a symmetric dielectric constant will be symmetric, and therefore will have a diagonal form.

The mentioned expansion method is called the *plane wave method* (PWM) and is formally described for a three-dimensional lattice in appendix A. The computational approach consists in defining a wave propagation vector $\vec{k}$ and solving the eigenvalue problem for truncated expansions. Using standard diagonalisation routines, eigenvalues and eigenvectors are found: the first correspond to the frequencies of the wave, while the latter define the amplitudes of the field projections on the basis of plane wave harmonics.

In this way, sets of eigenvalues are found for each wave vector. Varying the wave vectors over the whole *Brillouin* zone, one obtains bands of frequencies, which describe the propagation of waves within the periodic structure. The inset of figure 2.3 shows an example of band diagram including two bands with a scaled wave vector component and the frequency on the horizontal and vertical axes, respectively. This technique solves *Helmoltz* (or *Maxwell*'s) equations for all the chosen values of the wave vector within the periodic structure and enables one to perform an analysis of the propagation of waves excited externally by a monochromatic field, when for a given frequency, the corresponding wave vectors of the propagating waves are extrapolated from the diagram. The external field can couple to one or more bands, or alternatively to none when its frequency falls within a range of frequencies for which no wave vector value is available, that is within a complete bandgap. The field can be reconstructed by feeding the coefficients of the eigenvectors back into the expansion forms.

2.1.3 The rectangular lattice

Since scientists' efforts in computing the band structure of photonic crystals (PCs) has mainly been aimed at obtaining complete bandgaps, the structures investigated in the field of PCs usually had lattice vectors of comparable length. Lattices with substantially different periods are characterised by the crossing of lower bands than the more structurally homogeneous PCs, a property due to the large difference in periods along different directions which also causes bandgaps to be incomplete due to the large variation in the frequency of the modes at the edge of the *Brillouin* zone. Interesting optical properties of rectangular lattices have been recently discussed by Bewley *et. al.* [91] in an investigation of PC distributed-feedback lasers operating at mid-infrared wavelengths. Bewley *et. al.* modelled a low-modulation rectangular PC with cylindrical elements and a ratio of the lattice constants of 2.6.

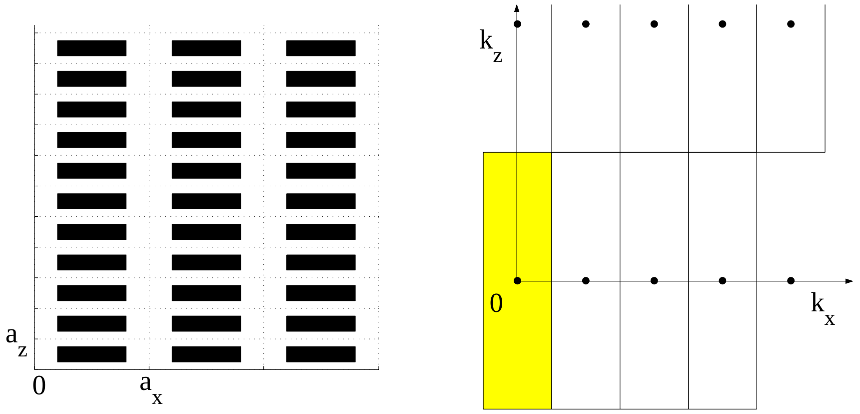

Figure 2.1: Plots of the dielectric arrangement (left-hand side) and its reciprocal lattice (right-hand side). The *Brillouin* zone including $\vec{k} = (0, 0)$ is highlighted in yellow.

Here, an original study of the band diagram of a rectangular lattice of rectangular dielectric elements embedded in vacuum (or air) is presented in some detail. This arrangement is an important constituent of the *Morpho* microstructure and its role in the mechanisms of colour production on the wings of the butterfly will be discussed in chapter 6. The structure considered has an index of refraction of 1.56, a long period of $675nm$ and a corresponding linear filling fraction of 0.6, and a short period of $180nm$ with a corresponding linear filling fraction of 0.5, which results in an area filling fraction of 0.3. Let the plane of the two-dimensional representation be xz, the coordinate axes $\hat{x}$ and $\hat{z}$ coincide with the orthogonal lattice vectors, and a_x and a_z be the long and short periods, respectively. The arrangement of dielectric is shown in the plot on the left-hand side of figure 2.1. The reciprocal lattice and the *Brillouin* zones are rectangular, as illustrated in the plot on the right-hand side of figure 2.1. The reciprocal space is tiled with the zones on a pattern determined by the reciprocal lattice.

The eigenvalues of the problem resulting from the concatenation of the inhomogeneous *Maxwell*'s equations and defined in equation 2.1 were obtained using a two-dimensional PWM with 81 terms in the field and dielectric function expansions. The formalism of this method is presented in appendix A.

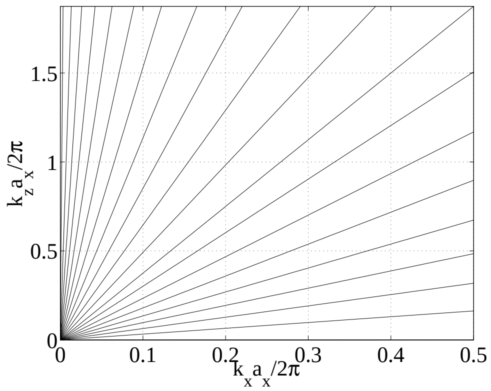

Figure 2.2: Schematic of the radial scan of the reduced *Brillouin* zone performed by the PWM band solver.

An investigation of the propagation properties of a periodic structure requires establishing with precision its band structure, a problem solved straightforwardly with the PWM up to the point of obtaining a set of values for each computed point in the reciprocal space. The task of ordering these values into bands consists of determining to which *Brillouin* zone a computed value belongs. Where for most of locations this can be done easily by studying the coefficients of the field eigenvectors or relating via the continuity of a band surface a point of the reduced *Brillouin* zone to other locations (for example the origin), where the analysis of the eigenvectors is trivial. This method however is not applicable for points where two bands cross. In those cases, as at the edges of the zone, the projections of the field on the expansion basis for different eigenvalues are equivalent and the band surfaces are discontinuous, as will be shown below. An algorithm that splits the task of ordering the eigenvalues in two manageable procedures has been developed and will be presented in this section: first the eigenvalues are pre-ordered on the principle that all the points of a band lie on a continuous surface; then, by comparing the coefficients of the field eigenvectors of these pre-ordered sets, piecewise continuous surfaces are sorted and the real bands are obtained.

The reduced *Brillouin* zone was scanned radially, varying the wave vector magnitude from 0 to the edge of the zone for several directions of propagation

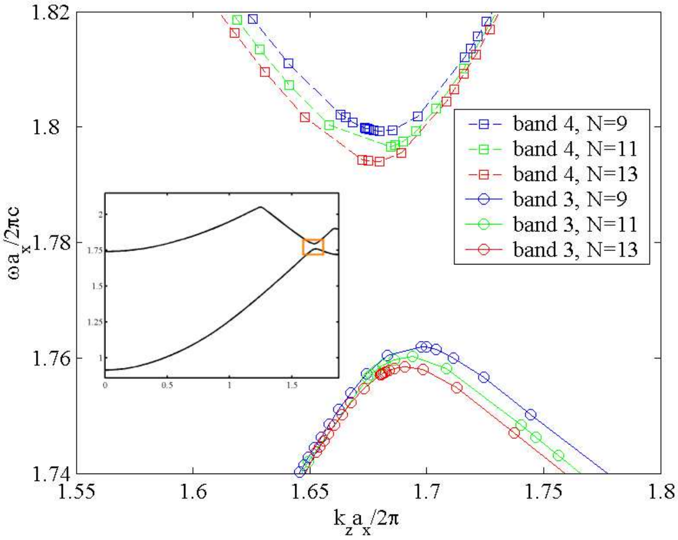

Figure 2.3: Band diagram of a rectangular two-dimensional periodic structure for a TM polarised field computed with the PWM. The angle of propagation with respect to $\hat{z}$ was $\angle(\vec{k}, \hat{z}) = 0.57°$, and units are scaled.

as represented in the plot of figure 2.2. An iterative approach was used to obtain the necessary resolution where the bands are strongly curved and particularly where the frequency values of two bands are very close. With this method, the increment in wave vector magnitude, to progress from one computed point in the reciprocal space to the next along each computed direction of propagation, was controlled via a feedback process, to ensure the continuity of the curve of the ordered sets. Figure 2.3 shows the detail of a band calculation for a TM polarised field in a region of the reciprocal space where two bands have close values (the angle of propagation with respect to $\hat{z}$ was $\angle(\vec{k}, \hat{z}) = 0.57°$). The computed values for the third and fourth band are depicted for the region of normalised wave vector component k_z around $\frac{k_z a_x}{2\pi} = 1.7$. The inset shows the pre-ordered sets on the entire extension of the *Brillouin* zone along the same direction. The high resolution obtained with the iterative method clearly shows the anti-crossing behaviour of the frequency eigenvalues, which leaves a gap in the range of frequencies that can propagate in the periodic structure. The dependence of the values of the

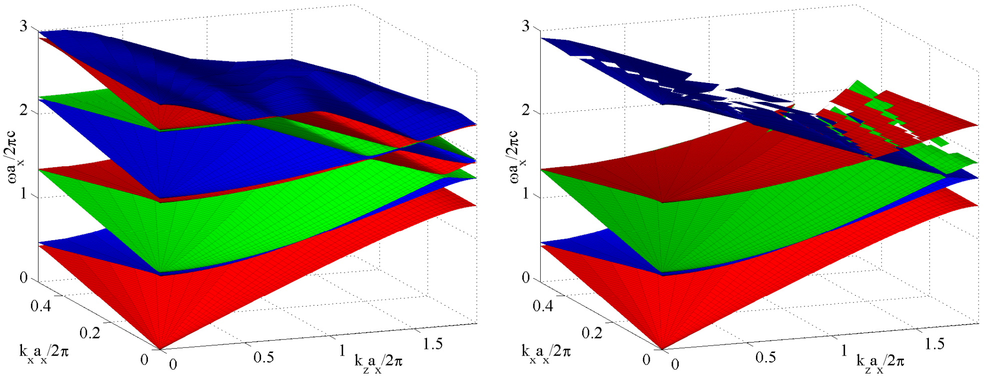

Figure 2.4: Two-dimensional eigenvalue diagram of a rectangular two-dimensional periodic structure for TM polarisation computed with the PWM. The plot on the left-hand side shows the pre-ordered sets. Ordered dielectric bands are shown in the plot on the right. Units are scaled.

third and fourth band at the gap ($\frac{k_z a_x}{2\pi} = 1.68$) on the number of terms used in the expansion was investigated, in order to assess the truncation error arising from the use of 81 terms. Progressively increasing the number of terms in the expansion up to 961 resulted in a down-sloping behaviour of the eigenvalues of both bands, tending (saturating) towards the constant values of 1.753 and 1.787 for the third and fourth band, respectively. Using only 81 terms, the truncation error for both bands, and therefore for the size of the gap, was 0.7%. Consequently, the observed gap is not a numeric artefact and has a relative width of 1%. The plot on the left-hand side of figure 2.4 shows the first eight sets of pre-ordered eigenvalues for the mentioned rectangular structure and all directions of propagation.

An analysis of the distribution of the field intensity amongst the various coefficients of the eigenvectors away from the point where the gap occurs permits ordering of different parts of the pre-ordered sets of eigenvalues to their band. Table 2.1 shows the first three normalised coefficients of the expansion for each orthogonal lattice direction for the third and fourth pre-ordered sets, and for values of the wave vector component $\frac{k_z a_x}{2\pi} = 1.65$ and 1.75. These correspond to the example shown in figure 2.3. Boldface numbers mark the coefficient with the largest absolute value. For the larger value of k_z, the eigenvector pre-ordered to the fourth band has the same field distribution of that pre-ordered to the third band for the smaller wave vector value. The opposite is true for the two remaining eigenvectors. The same results are found for all points either side of the gap and consequently piecewise continuous segments of the pre-ordered sets are swapped between different sets to produce the ordered bands. Once this procedure is applied to all points of the *Brillouin* zone, a band diagram is obtained with piecewise continuous band surfaces. The plot on the right-hand side of figure 2.4 shows five ordered bands for the calculated example. Discontinuities of the band surfaces and the corresponding gaps where bands approach are clearly visible there.

Both the frequency and the tangential component of the wave vector in a layered arrangement of dielectrics are quantities conserved by waves propagating throughout the structured material. This allows us to study the propagation of externally excited waves within the PC. An impinging monochromatic wave of frequency ω and having a tangential component k_x can couple to one or more *Bloch* modes. For the band of a coupled mode,

Table 2.1: Normalised coefficients of the eigenvectors of the pre-ordered third and fourth band for two values of the wave vector component k_z either side of the gap depicted in figure 2.3. Only nine coefficients of the 81-terms expansion are shown for each orthogonal lattice direction, which correspond to the *Brillouin* zones closest to $\vec{k} = (0, 0)$. Boldface numbers mark the coefficient with the largest absolute value.

$\frac{k_z a_x}{2\pi} = 1.65$

band 3			band4		
0.1042	0.2730	0.1251	−0.3003	**−0.7613**	−0.2814
−0.5106	0.4966	**−0.5949**	−0.3015	−0.1694	−0.3121
−0.0131	0.0031	−0.0199	−0.0377	−0.0488	−0.0488

$\frac{k_z a_x}{2\pi} = 1.75$

band 3			band4		
0.2699	**0.7514**	0.2738	−0.0599	−0.1618	−0.0144
0.0430	0.5177	0.0039	−0.6042	0.3382	**−0.6545**
0.0302	0.0515	0.0268	−0.0328	−0.0222	−0.0365

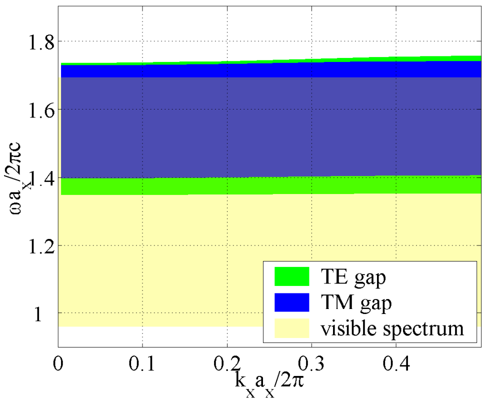

Figure 2.5: Plots of the gap between bands belonging to the first class of *Brillouin* zones for TE and TM polarisations with the visible range of wavelengths.

extraction of a normal component k_z for which the band has the value ω determines a wave vector $\vec{k} = (k_x, k_z)$ for the central term in the field expansion, and the corresponding eigenvector provides its coefficients. Each mode decomposes in a set of harmonic waves propagating in directions obtained from $\vec{k}$ and the reciprocal lattice vectors.

At the edges of a *Brillouin* zone the amplitude of forward and backward propagating waves is equal and their superposition results in standing waves, whereby the power of the mode is reflected by the zone boundary, a phenomenon called *Bragg* reflection. As a result of this condition a gap is formed between the bands at the boundary of neighbouring zones (a bandgap). For frequencies within the gap, the mode is evanescent, it only exists at a termination of the PC and the impinging power coupled to it is fully reflected. The bandgap of the rectangular lattice under investigation at the far side of the reduced *Brillouin* zone is shown in figure 2.5 for both polarisations. The long-wavelength edge is flat in both cases and is found at normalised frequency values of 1.35 and 1.40 for TE and TM polarisation, respectively. This means that, irrespectively of the angle of incidence, the field coupled to this mode will be totally reflected at frequencies higher than that threshold. Other bandgaps are found at higher frequencies.

In the normalised units used in all presented graphs, the visible spectrum extends from 0.96 to 1.69. This places the lowest bandgap at visible wavelengths for the studied arrangement, while the lowest gap due to bands crossing inside the zone is found at a value 1.8, which is outside of the visible range. Scaling up the dimensions of the lattice by only 7% shifts this gap and brings it in the visible range, and shifts the long-wavelength edge of the main bandgap to longer wavelengths (for example from 482 to 514nm for TM polarisation). Decreasing the filling fraction of the structure lowers its average index of refraction and shifts all band values at the edge of the reduced *Brillouin* zones to shorter wavelengths (for example the long-wavelength band edge of the lowest TM bandgap to 397nm for a lateral linear filling fraction of 0.18).

2.1.4 The centred rectangular lattice

Using the method presented in section 2.1.3, a centred rectangular lattice of rectangular dielectric elements having an index of refraction of 1.56 and embedded in vacuum (or air) was also investigated for the first time. The optical properties of this arrangement and of the rectangular lattice will contribute to the discussion of the mechanisms of colour production on the wings of *Morpho rhetenor* presented in chapter 6. The structure is periodic along the x and z directions with respective periods of 675 and 180nm, but each rectangular cell contains two elements. The dimensions of the elements are 202.5 and 90nm in the x and z directions respectively, which results in an area filling fraction of 0.3, a value equal to the rectangular structure presented above. The arrangement of dielectric is shown in the plot on the left-hand side of figure 2.6. The reciprocal lattice and the *Brillouin* zones are irregular hexagonal, as depicted in the plot on the right-hand side of figure 2.6. Two substantial differences emerge when comparing the *Brillouin* zone of the centred lattice with that of the rectangular one: (i) the first is twice the size of the second in k_x direction; (ii) the far side of the hexagonal zone is at an angle (14.9°) with the k_x direction, while for the rectangular

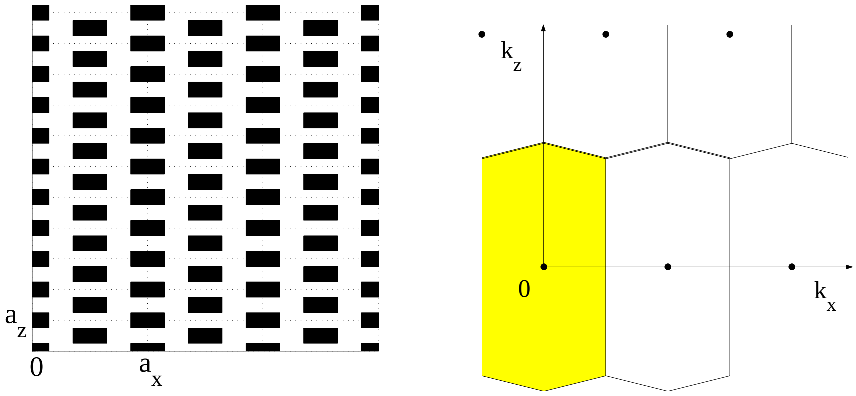

Figure 2.6: Plots of the dielectric arrangement (left-hand side) and its reciprocal lattice (right-hand side). The *Brillouin* zone including $\vec{k} = (0, 0)$ is highlighted in yellow.

one they are parallel.

A bandgap is found for the rectangular lattice at $\frac{k_x a_x}{2\pi} = 0.5$, the edge of the rectangular *Brillouin* zone, but none occurs there for the centred rectangular lattice, since the edge of the hexagonal zone is at a value of 1. Figure 2.7 shows the lowest band of the centred structures for both polarisation and illustrates the absence of gaps within the zone (to be compared with figure 2.4). For the hexagonal lattice, the gaps at the near side of the *Brillouin* zone are sensibly larger than for the rectangular one; for example, at $\vec{k} = \frac{2\pi}{a_x}(1, 0)$ and for the TM polarisation one gap is 70% larger than the other.

Evanescent modes are reflected by the zone boundaries and the inclination of the far side of the hexagonal zone causes a transfer of the incident power into expansion terms propagating backwards along both axes of the reciprocal space. This is in contrast with the rectangular zone, for which the modes are only reflected along the k_z axis.

The bandgap of the centred rectangular lattice at the far side of the first *Brillouin* zone is shown in figure 2.8 for both polarisations. The long-wavelength edge is flat in both cases and is found at normalised frequency values of 1.45 and 1.56 for TE and TM polarisation, respectively. This

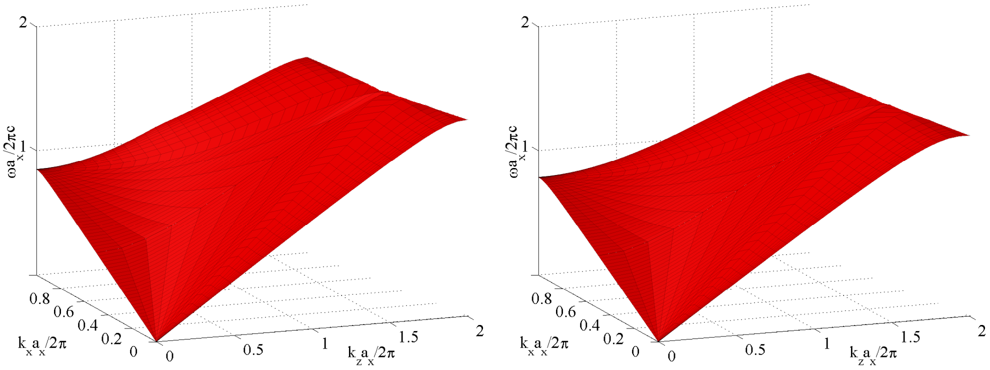

Figure 2.7: Two-dimensional diagram of the lowest band of a centred rectangular two-dimensional periodic structure computed with the PWM. The plot on the left-hand side shows the band for the TM polarisation, while the TE polarisation is shown on the right-hand side. Units are scaled.

means again that, irrespectively of the angle of incidence, the field coupled to this mode will be totally reflected at frequencies higher than that threshold. Other bandgaps are found at higher frequencies.

It was mentioned in section 1.6.1 how the diffraction of two-dimensional photonic crystals was accurately calculated by Sakoda [57] using expansion methods, but it is clear that the validity of this approach should be proved for each individual case, since it relies on the choice of a suitable expansion basis and a truncation order. In fact, if a terminated lattice occurs, the operator Θ of equation 2.1 is not *Hermitian*, therefore its eigenvalues are not real and its eigenvectors cannot be projected on an orthogonal basis in a definite way.

For this reason, it is not possible to quantitatively model the diffraction of terminated periodic structures using the presented expansion method. Different numerical methods were used to compute the diffraction efficiencies of models of the *Morpho* microstructure. These methods are presented below. First, the theory of diffraction of periodic structures is introduced with the intention to discuss the foundations of the numerical methods.

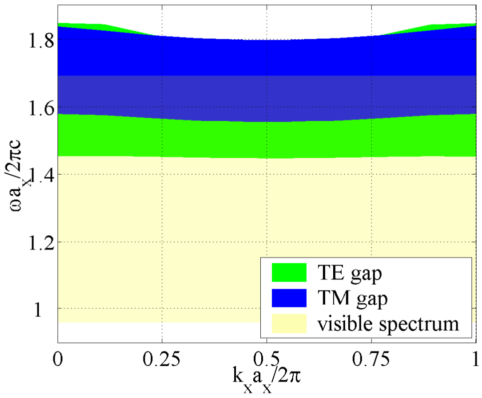

Figure 2.8: Plots of the gap between bands belonging to the first class of *Brillouin* zones for TE and TM polarisations with the visible range of wavelengths.

2.2 Diffraction

The *Fresnel-Kirchhoff* diffraction integral [32] gives an approximate solution of the *Helmholtz* equation at an arbitrary point in space, in terms of the values of the solution and its derivatives on an arbitrary surface. *Kirchhoff*'s theory of diffraction is exact for a closed surface. It is often only possible to know the values of the field over an open surface but not over the whole of a closed one, for this reason *Kirchhoff's boundary conditions* are introduced. These neglect the field and its derivative along the normal on the rest of a closed surface which includes the open one, thus the system is regarded as if the surface of known field were a window in an otherwise opaque screen. With this transformation, once *Maxwell*'s equations are solved in and around the periodic medium, the diffracted field from a periodic structure at any point in space can be determined. These arguments will be discussed in more detail below.

First of all for two differentiable scalar fields U and V, such that both are eigenvectors of the *Helmholtz* equation, *Green*'s theorem applies,

$$\int_{\partial\Omega} (U\hat{n} \cdot \nabla V - V\hat{n} \cdot \nabla U)\, da = 0,$$

where Ω is a portion of space, $\partial\Omega$ its surface, $\hat{n}$ the inward normal to the surface, and da denotes a surface integral. If one field, say U, is the object of the investigation and V is chosen to be the free-space *Green*'s function, *Kirchhoff*'s integral is obtained straightforwardly with few manipulations through extending and splitting $\partial\Omega$ in two, such that the surface of integration envelops an arbitrary point in space $\vec{r}_0$ confined in Ω:

$$U(\vec{r}_0) = \int_{\partial\Omega} (U\hat{n} \cdot \nabla V - V\hat{n} \cdot \nabla U)\, da, \quad V(\vec{r}, \vec{r}_0) = \frac{e^{ik_0|\vec{r}-\vec{r}_0|}}{4\pi|\vec{r} - \vec{r}_0|},$$

where $\vec{r}$ indicates the locus of the integration and k_0 the vacuum wave number of the field U. To derive a similar expression for a point $\vec{r}_0$ infinitely far away, the surface $\partial\Omega$ is made to stretch to infinity and integration is performed on a finite portion of it, considering *Kirchhoff*'s boundary conditions. However, applying this approximation, which requires the field and its derivative along $\hat{n}$ to take the value zero at least over a finite surface, one encounters an inconsistency, since those conditions imply that the field has the value zero everywhere in space. For a plane window, this inconsistency can be lifted using a different *Green*'s function as the field V,

$$V(\vec{r}, \vec{r}_0) = \frac{1}{4\pi} \left(\frac{e^{ik_0|\vec{r}_0-\vec{r}|}}{|\vec{r}_0 - \vec{r}|} + \frac{e^{ik_0|\vec{r}_0-\vec{r}_1|}}{|\vec{r}_0 - \vec{r}_1|} \right),$$

where $\vec{r}_0$ is again an arbitrary point in space and $\vec{r}_1$ its mirror image with respect to the plane of the surface. The derivative of V along $\hat{n}$ is zero for any point of the plane. In this way, the condition that the field be zero on the surface outside the window is not required anymore and the second condition alone is consistent with a non-zero field. For very large values of $|\vec{r} - \vec{r}_0|$, *i.e.* in the so-called *far-field*, the resulting integral expression for the field U is

$$U(\vec{r}_0) = \frac{k_0}{2\pi i} \int_S \frac{e^{ik_0|\vec{r}_0-\vec{r}|}}{|\vec{r}_0 - \vec{r}|} \hat{n} \cdot \frac{\vec{r}_0 - \vec{r}}{|\vec{r}_0 - \vec{r}|} U(\vec{r}) da,$$

where S denotes the surface generating the field.

To solve the diffraction of periodic structures working in the resonance domain of frequencies a scalar theory is inappropriate and the above equation must be applied at the same time to all components of the electromagnetic fields, which is the reason why the diffraction problem is solved in its full vectorial form even in low dimensional models. The vectorial form of the diffraction integral is as follows:

$$\vec{E}(\vec{r_0})=\frac{\mu_0\omega}{4\pi r_0 i}\int_S\left(\hat{r}_0\times\left(\hat{r}_0\times\left(\hat{n}\times\vec{H}(\vec{r})\right)\right)-\frac{1}{\mathrm{Z}_0}\hat{r}_0\times\left(\hat{n}\times\vec{E}(\vec{r})\right)\right)e^{ik_0(r_0-\hat{r}_0\cdot\vec{r})}da, \tag{2.3}$$

where r_0 is the magnitude of $\vec{r_0}$ and $\hat{r}_0$ its unit vector ($\vec{r_0}=r_0\hat{r}_0$), Z_0 is the impedance of vacuum and S is a plane surface.

For illustration purposes let us consider an electromagnetic field periodic in one direction on the surface S, say x. After substitution of the *Fourier* expansions,

$$\begin{array}{ll}\vec{E}(x)=e^{ik_{0x}x}\sum_p\vec{E}_p e^{ipbx}, & \vec{E}_p=(\vec{E}(x),e^{ipbx}),\\ \vec{H}(x)=e^{ik_{0x}x}\sum_p\vec{H}_p e^{ipbx}, & \vec{H}_p=(\vec{H}(x),e^{ipbx}),\end{array}$$

where k_{0x} is the x component of $\vec{k}_0$, and $\vec{E}_p$ and $\vec{H}_p$ are the *Fourier* coefficients of the electric and magnetic field, respectively, the above integral can be recast in the following way:

$$\vec{E}(\vec{r_0})=-i\frac{\mu_0\omega}{4\pi r_0}\mu(S)e^{ik_0r_0}\left(\hat{r}_0\times\left(\hat{r}_0\times\left(\hat{n}\times\vec{H}_p\right)\right)-\frac{1}{\mathrm{Z}_0}\hat{r}_0\times\left(\hat{n}\times\vec{E}_p\right)\right)$$

if $k_0\hat{r}_0\cdot\hat{x}=k_{0x}+pb$ for an integer value of p and $\vec{E}(\vec{r_0})=0$ otherwise. $\mu(S)$ is the area of the surface S. This results means that for given wave number k_0 and in-plane component of the propagation vector k_{0x}, the diffracted field is non-zero in far-field only for a set of specific directions. These are the *diffraction orders.*

The above integral is used in particular to calculate the far-field response (*i.e.* the diffraction efficiencies) of periodic structures with a plane surface, given an impinging plane wave of frequency ω incident at an angle θ_{inc} with respect to the surface normal. These conditions of incidence determine the parameters $k_0 = \omega/\mathrm{c}$ and $k_{0x} = k_0 sin(\theta_{inc})$, and the resulting diffraction condition for the orders is

$$\sin\theta_p = \sin\theta_{inc} + p\frac{b}{k_0},$$

which is called the *grating equation*.

A final note to *Kirchhoff*'s approximation is necessary here. The idealized condition of zero-valued derivatives of the fields along the normal to the opaque screen outside the surface of integration can be met by placing the window very close to the source of radiation, such that the radiated fields do not cross the rest of the infinitely extended surface. Care must be taken though, that evanescent, non-propagating fields from the source (say the surface of a periodic structure) be excluded from the integration. In the numerical implementation of *Kirchhoff*'s integral presented below all these issues were considered.

2.3 Numerical computation of the diffraction of layered photonic structures

In the previous sections, a method to solve *Maxwell*'s equations in a periodic medium and one to transform the field in its far-field resultant were presented. They enable one to study the diffraction properties of a periodic lattice in relation to its internal band structure, which is a source of valuable insight into the causes behind the far-field phenomenology. It was also mentioned though, how the expansion approach is approximate when a terminated lattice occurs and its validity should be proven from case to case. Additionally, the implementation of disorder, of arbitrary shapes of the "atomic" scatterers, or of any deviation from an arrangement periodic in as many dimensions as the modelling space require extremely detailed expansions.

For these reasons, solving the appropriate equations with the finite-difference time-domain (FDTD) method is often preferred to expansion methods. For an extensive review of the theory and applications the reader is referred to the books by Taflove [65] and Kunz [92].

2.3.1 Finite-difference time-domain method

It was mentioned in section 1.6.1 how the computation of several properties of photonic devices has been successfully achieved by solving approximatively *Maxwell*'s equations for propagating waves on a discrete mesh of points in space [66, 67]. The FDTD method is full-vectorial and, being in the time domain, also allows non-stationary regimes to be considered. The computational tool is generic and for different investigated arrangements only matrices containing information about the material properties and geometry are changed.

The mesh of points where the fields are calculated can be arranged arbitrarily and methods are available to perform the calculations on non-orthogonal meshes [67]. This allows the material arrangements to be mapped by the mesh in efficient ways in case increased resolution is desired along curved surfaces, but a degree of complexity is introduced in comparison to an orthogonal and uniform grid, which, in turn, is unspecific to the studied device. On such a grid the space is filled with cubic cells, or square ones in a two-dimensional model [92]. In a plane, say xz as in the example of figure 2.9, each point of the grid (x_i, z_j) – for the sake of brevity indicated by (i, j) in future – is at a constant distance Δs from its nearest neighbours, $(i-1, j)$, $(i+1, j)$, $(i, j-1)$ and $(i, j+1)$. The electric field $\vec{E}$ is calculated at the nodes of this grid and a second grid is defined for the magnetic field $\vec{H}$, entirely equal to the first one but "staggered" or shifted with respect to it by half a cell size along each space coordinate. In this representation the components of the magnetic field are placed at different locations on the surface of a cell, as it is shown in figure 2.9. Alternatively, both fields can be evaluated on the same grid, with a scheme defined as *collocated.*

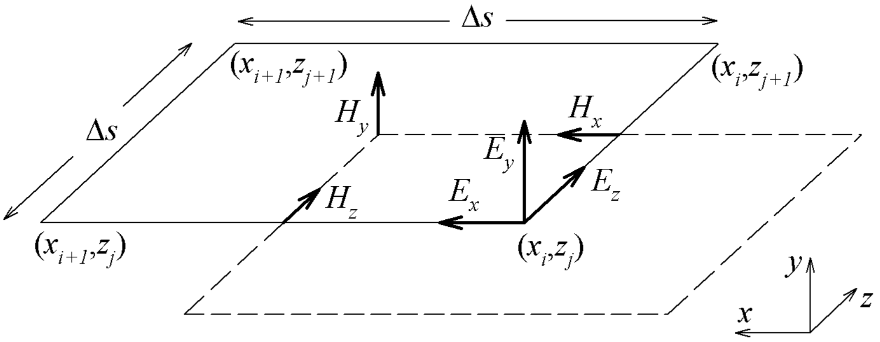

Figure 2.9: Illustration of discretisation of fields on a two-dimensional grid for FDTD computations.

The inhomogeneous *Maxwell* equations for charge-free, current-free and non-magnetic materials are written as follows:

$$\begin{aligned} \nabla \times \vec{H}(\vec{r},t) &= \varepsilon(\vec{r})\epsilon_0 \frac{\partial \vec{E}}{\partial t}(\vec{r},t), \\ \nabla \times \vec{E}(\vec{r},t) &= -\mu_0 \frac{\partial \vec{H}}{\partial t}(\vec{r},t). \end{aligned} \tag{2.4}$$

In a two-dimensional system, say with continuous translation symmetry in the y direction, the translation invariance implies that the field derivatives along the y axis disappear. Equations 2.4 therefore reduce to the following set of partial differential equations:

$$\begin{aligned} \mu_0 \frac{\partial H_x}{\partial t} &= \frac{\partial E_y}{\partial z}, & \mu_0 \frac{\partial H_y}{\partial t} &= -\left(\frac{\partial E_x}{\partial z} - \frac{\partial E_z}{\partial x}\right), \\ \mu_0 \frac{\partial H_z}{\partial t} &= -\frac{\partial E_y}{\partial x}, & \varepsilon\epsilon_0 \frac{\partial E_x}{\partial t} &= -\frac{\partial H_y}{\partial z}, \\ \varepsilon\epsilon_0 \frac{\partial E_y}{\partial t} &= \left(\frac{\partial H_x}{\partial z} - \frac{\partial H_z}{\partial x}\right), & \varepsilon\epsilon_0 \frac{\partial E_z}{\partial t} &= \frac{\partial H_y}{\partial x}. \end{aligned} \tag{2.5}$$

The time variable t is equally discretised by introducing a succession of time steps Δt. The fields are therefore evaluated at the nodal points

(i, j, n), where the index n refers to the n^{th} time step. The magnetic field is evaluated half a time step away from the electric one, formally $\vec{H}\,(i, j, n+\frac{1}{2})$, which allows marching in time of the fields. This happens with a pattern called *leapfrog time-stepping* [65], because the fields half a time step away are related by equations 2.5, as will be shown explicitly below, and the magnetic field skips the time nodes of the electric field and viceversa.

With the FDTD method the partial derivatives of the equations are approximated by finite difference (FD) terms at each point on the grid. This results in a set of six FD equations to be solved simultaneously for all points on the grid. In a two-dimensional model the two polarisations, TM and TE, are propagated independently and only three field components and equations are necessary to solve the problem for each polarisation. The TM problem is solved for H_y, E_x and E_z with the right-hand side column of equations 2.5, while the TE problem is solved for E_y, H_x and H_z with the left-hand side column. Several differencing schemes can be used and a so-called forward difference one will be considered here. For example, the spatial derivative with respect to x of the field component E_y at the point $(i+\frac{1}{2}, j, n)$ is represented as

$$\frac{\partial E_y}{\partial x}\,(i+\tfrac{1}{2}, j, n) = \frac{E_y(i+1, j, n) - E_y(i, j, n)}{\Delta s}.$$

Analogous definitions are made for all field components. The temporal derivative of the field component H_z is instead represented as

$$\frac{\partial H_z}{\partial t}(i, j, n) = \frac{H_z\,(i, j, n+\frac{1}{2}) - H_z\,(i, j, n-\frac{1}{2})}{\Delta t}.$$

Again, analogous expressions are defined for all field components.

Both these derivatives are evaluated at the same point in space (*cf.* figure 2.9) and substitution in equations 2.5 together with the other expressions, with the additional introduction of the parameter $\Delta\tau = \mathrm{c}\Delta t$, yields for the magnetic field components:

$$\begin{aligned}
H_x\,(i,j,n{+}\tfrac{1}{2}) &= H_x\,(i,j,n{-}\tfrac{1}{2}){+}\frac{\Delta\tau}{\mathrm{Z}_0\Delta s}\Big(E_y(i,j{+}1,n){-}E_y(i,j,n)\Big),\\
H_y\,(i,j,n{+}\tfrac{1}{2}) &= H_y\,(i,j,n{-}\tfrac{1}{2}){+}\frac{\Delta\tau}{\mathrm{Z}_0\Delta s}\Big(E_x\,(i{+}\tfrac{1}{2},j,n) - E_x\,(i{+}\tfrac{1}{2},j{+}1,n){+}\\
&\qquad {+}E_z\,(i{+}1,j{+}\tfrac{1}{2},n){-}E_z\,(i,j{+}\tfrac{1}{2},n)\Big),\\
H_z\,(i,j,n{+}\tfrac{1}{2}) &= H_z\,(i,j,n{-}\tfrac{1}{2}){+}\frac{\Delta\tau}{\mathrm{Z}_0\Delta s}\Big(E_y(i{-}1,j,n){-}E_y(i{+}1,j,n)\Big),
\end{aligned}$$

whereby the average of a field component over two neighbouring cells $u\,(i{\pm}\tfrac{1}{2},j,n) = \tfrac{1}{2}\Big(u(i{\pm}1,j,n) + u(i,j,n)\Big)$ is used to generate coincident functions where necessary. On the other hand one obtains for the electric field:

$$\begin{aligned}
E_x(i,j,n{+}1) &= E_x(i,j,n){+}\frac{\mathrm{Z}_0\Delta\tau}{\Delta s\varepsilon(i,j)}\Big(H_y\,(i{-}\tfrac{1}{2},j{-}1,n{+}\tfrac{1}{2}){-}\\
&\qquad {-}H_y\,(i{-}\tfrac{1}{2},j,n{+}\tfrac{1}{2})\Big),\\
E_y(i,j,n{+}1) &= E_y(i,j,n){+}\frac{\mathrm{Z}_0\Delta\tau}{\Delta s\varepsilon(i,j)}\Big(H_x\,(i,j,n{+}\tfrac{1}{2}) - H_x\,(i,j{-}1,n{+}\tfrac{1}{2}){+}\\
&\qquad {+}H_z\,(i{-}1,j,n{+}\tfrac{1}{2}){-}H_z\,(i,j,n{+}\tfrac{1}{2})\Big),\\
E_z(i,j,n{+}1) &= E_z(i,j,n){+}\frac{\mathrm{Z}_0\Delta\tau}{\Delta s\varepsilon(i,j)}\Big(H_y\,(i,j{-}\tfrac{1}{2},n{+}\tfrac{1}{2}){-}\\
&\qquad {-}H_y\,(i{-}1,j{-}\tfrac{1}{2},n{+}\tfrac{1}{2})\Big).
\end{aligned}$$

The presented differential method is accurate to the second order both in time and space [65] and as such, stability criteria have to be respected when implementing it in order to prevent the FDTD equations from becoming unbound and unstable. This is achieved by making sure the field components do not vary by more than 10% between neighbouring cells. For the case treated above the stability criteria for the space and time step are $\Delta s \leq \lambda/10$ and $\Delta\tau/\Delta s \leq 1/\sqrt{2}$, respectively [53].

These criteria can be rather stringent in some cases and higher order accuracy schemes might be required to achieve better accuracy with coarse grids or to shorten computation times. For example, using a fourth order polynomial $P(i,j)$ to represent a field component u by interpolation through the two nearest neighbours either side of the considered node, one obtains an expression for the derivative as follows:

$$\frac{\partial P}{\partial x}(i,j) = -\frac{u(i{+}2,j) - 8u(i{+}1,j) + 8u(i{-}1,j) + u(i{-}2,j)}{12\Delta s},$$

which is an approximation of the derivative with fourth order accuracy. Different polynomial expansions are possible and the choice of a particular one depends on the adopted differencing scheme [65]. Implementation of high order time stepping schemes is very computationally expensive, since interpolation through values over entire grids at successive time steps are necessary, and therefore the gain due to a higher numerical accuracy is lost in the longer computational time involved.

In presence of strongly modulated dielectric constants further improvements to the accuracy of the numerical method can be achieved by replacing the discontinuous dielectric with a smoothed one. An efficient way of doing this consists of approximating the value of the dielectric constant at a node using the values at the nearest neighbours. Writing the *Taylor* expansion of the dielectric function up to the second order

$$\begin{aligned}\varepsilon(x{+}\Delta x, z{+}\Delta z) = {} & \varepsilon(x,z) + \left(\frac{\partial \varepsilon}{\partial x}(x,z)\Delta x + \frac{\partial \varepsilon}{\partial z}(x,z)\Delta z\right) + \\ & + \frac{1}{2}\left(\frac{\partial^2 \varepsilon}{\partial x^2}(x,z)\Delta x^2 + \frac{\partial^2 \varepsilon}{\partial x^2}(x,z)\Delta x^2 + 2\frac{\partial^2 \varepsilon}{\partial x \partial z}(x,z)\Delta x \Delta z\right)\end{aligned}$$

and adding the expansions around the node (i,j) for the four nearest neighbours, the following expression is obtained

$$\left(1 + \frac{\Delta s^2}{4}\nabla^2\right)\varepsilon(i,j) = \frac{\varepsilon(i{-}1,j) + \varepsilon(i{+}1,j) + \varepsilon(i,j{-}1) + \varepsilon(i,j{+}1)}{4},$$

where ∇ is the nabla operator. In the summation over the nodes the first derivatives of the four expansions add to zero and the mixed second derivatives disappear for all nodal points. After discretisation of the second derivatives and once written in matrix form, this results in a tri-diagonal, antisymmetric matrix operator multiplying the dielectric matrix on the left hand side of the equation and the sum of the four shifted dielectric matrices on the right. The smoothed dielectric constant matrix is obtained via inversion of the operator.

Despite all these measures to reduce computational errors, the approximate solution of the differential equations always results in a phase dispersion error [53, 65] and consequently in numerical diffusion of the waves.

The necessity to reduce the space over which the computation is performed requires imposing boundary conditions to the FD equations. To compute the waves propagation in unbound regions it is necessary to introduce absorbing boundary conditions, such that the extension of the grid to infinity be simulated. This is done by adding a rim of several cells around the chosen space portion where impinging waves are extinguished without reflection for all angles of incidence. This is achieved with a so called *perfectly matched layer* (PML) as an absorbing medium, which consists of a uniaxial (anisotropic) electric and magnetic conductor [93]. In such a material no charges exist and the electric current $\vec{j_e}$ is described with the electric conductivity tensor σ_{kl} by $\vec{j_e} = \sigma_{kl}\vec{E}$, while the magnetic current $\vec{j_m}$ is described with the magnetic conductivity tensor τ_{kl} by $\vec{j_m} = \tau_{kl}\vec{H}$. For plane waves of frequency ω propagating in the direction $\hat{k}$, the wave vector is written as follows:

$$\vec{k} = k_0\sqrt{\left(\varepsilon + i\frac{\sigma_{kl}}{\omega\varepsilon_0}\right)\left(1 - i\frac{\tau_{kl}}{\omega\mu_0}\right)}\hat{k},$$

where k_0 is the vacuum wave number of $\vec{k}$ and ε is the dielectric constant of the material. With all tensor components equal zero except the one along the normal to the PML denoted by $\sigma_\perp$ and $\tau_\perp$, the field decays exponentially with distance from the layer surface. A condition of no reflection at the interface with such a medium is achieved if the following relation is fulfilled:

$$\frac{\sigma_\perp}{\varepsilon_0 \varepsilon} = \frac{\tau_\perp}{\mu_0}.$$

However, errors generated by the discretisation of the equations in the absorbing medium give rise to a reflection at each successive plane of nodal points. To tackle this problem a geometric profile for the electric conductivity is applied which is typically defined as follows [65]:

$$\sigma_\perp(d) = \sigma_0 g^{\frac{d}{\Delta s}}.$$

Where σ_0 is a very low conductivity, d is the penetration depth within the PML and g is a geometric factor. In this way, reflection is minimized when the field have large magnitudes, but efficient absorption is achieved due to the increasing value of the conductivity with growing penetration depth. One has to be careful that the extinction of the field does not exceed the numerical stability criteria and a sufficient thickness of the PML has to be chosen in order to extinguish the fields effectively.

The implementation of the PML boundary conditions is easily achieved using a split-field representation of the *Maxwell*'s equations [93]. The transversal components of the fields in a two-dimensional model are separated in two parts, each travelling along one of the orthogonal directions of the grid. The fields then eventually impinge on a PML normally and are absorbed. This results in defining four sets of differential problems with their respective initial conditions.

Different initial conditions can obviously be implemented. A particularly useful one consists in defining a *Gaussian* wavepacket taking care of the required phase shift of half a time step between the electric and magnetic field components [53]. This allows to propagate a signal with a wide bandwidth in the frequency domain and therefore to extrapolate the required information for all the frequencies included.

The final component of an FDTD computation routine is the sampling of the field, which is specific to the required computational results. To obtain the far-field response of a device, a complete sampling of the scattered field is necessary. This is done by measuring the field values at a surface within the grid at all times during the computation making sure that the initial pulse has been completely scattered and transited through the surface. The sampling surface must not be too close to the device to avoid measuring evanescent fields, which do not propagate. However, keeping it at a distance from the sample means that not all of the scattered fields travelling normally to the window are necessarily sampled and the computation of the diffraction from the device does not satisfy *Kirchhoff*'s approximation. The sampling surface must therefore envelop the whole device.

Figure 2.10 shows the computation field and the components of a typical FDTD computation.

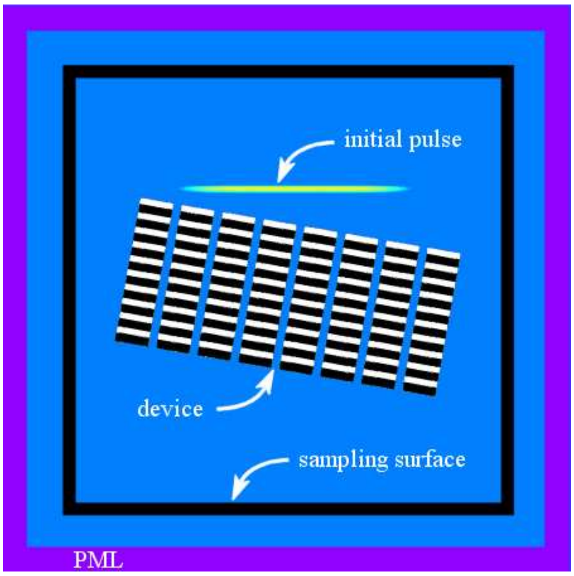

Figure 2.10: Computation field and components of a typical FDTD computation. A grid of points where the material properties are defined and the propagating fields are computed fills the represented space. Varying material properties, *i.e.* dielectric constant and conductivities, define the background medium, the investigated device and the boundary conditions (PML). The initial condition, a *Gaussian* wavepacket is also shown.

2.3.2 Near-field to far-field transformation

The diffracted fields in their far-field representation are obtained via a near-field to far-field transformation (NFFFT), an operation that can be performed in both the frequency domain and the time domain. In the first case, once the diffracted field in an FDTD computation is sampled, it is *Fourier*-transformed into its frequency-domain expression at each sampled point on the sampling surface and the diffraction is successively obtained using equation 2.3. On the other hand, directly performing the NFFFT of the FDTD results in the time-domain permits reduction of the computational workload for the ensuing *Fourier*-transformation, since this step is executed only for a selection of angles of propagation, say 360, and not for the total sum of sampling points, which can amount to thousands. The counterpart of equation 2.3 in the time domain and in a two-dimensional model is as follows:

$$\vec{E}(\vec{r_0})=\frac{C}{r_0}\int_\Gamma\left(\hat{r}_0\times\left(\hat{r}_0\times\frac{\partial}{\partial t'}\left(\hat{n}\times\vec{H}(\vec{r},t')\right)\right)-\frac{1}{\mathrm{Z}_0}\hat{r}_0\times\frac{\partial}{\partial t'}\left(\hat{n}\times\vec{E}(\vec{r},t')\right)\right)d\gamma.$$

where C is a constant normalisation factor, $t' = t - \frac{r_0 - \hat{r}_0\cdot\vec{r}}{\mathrm{c}}$ is the retarded time, and r_0 and $\hat{r}_0$ are the magnitude and the unit vector of $\vec{r_0} = r_0\hat{r}_0$. Let us consider a TM polarised field sampled at the grid points $(i_0, j_1), \ldots, (i_0, j_P)$ and an angle of scattering θ. These conditions result in the following expressions for the electric and magnetic field, the sampling surface normal, and the normalised position vector, respectively:

$$\vec{E}=\begin{pmatrix}E_x\\0\\E_z\end{pmatrix},\quad \vec{H}=\begin{pmatrix}0\\H_y\\0\end{pmatrix},\quad \hat{n}=\begin{pmatrix}1\\0\\0\end{pmatrix},\quad \hat{r}_0=\begin{pmatrix}cos(\theta)\\0\\sin(\theta)\end{pmatrix}.$$

The time derivatives of the field components parallel to the sampling window plane are

$$\frac{\partial E_z}{\partial t}\,(i,j,n+\tfrac{1}{2}) \;=\; \frac{E_z(i,j,n+1)-E_z(i,j,n)}{\Delta t},$$

$$\frac{\partial H_y}{\partial t}(i,j,n) \;=\; \frac{H_y\,(i,j,n{+}\frac{1}{2}) - H_y\,(i,j,n{-}\frac{1}{2})}{\Delta t}.$$

The fields must be sampled at the same time and therefore the average between two following time steps is taken for the magnetic field

$$\frac{\partial H_y}{\partial t}\,(p,n{+}\tfrac{1}{2}) = \frac{1}{2}\left(\frac{\partial H_y}{\partial t}(i,j,n{+}1) + \frac{\partial H_y}{\partial t}(i,j,n)\right).$$

Integration is performed at coinciding places for both field components and due to the staggering of the fields, an estimated value for the derivative of E_z is obtained from the following average

$$\begin{aligned}\frac{\partial E_z}{\partial t}\,(p,n{+}\tfrac{1}{2}) \;=\;& \frac{1}{4}\Bigg(\frac{\partial E_z}{\partial t}\,(i,j,n{+}\tfrac{1}{2}) + \frac{\partial E_z}{\partial t}\,(i{+}1,j,n{+}\tfrac{1}{2}) + \\ &+\frac{\partial E_z}{\partial t}\,(i,j{+}1,n{+}\tfrac{1}{2}) + \frac{\partial E_z}{\partial t}\,(i{+}1,j{+}1,n{+}\tfrac{1}{2})\Bigg)\end{aligned}$$

In both these expressions the index p indicates a point in space with coordinates $(i_0, j_p{+}\frac{1}{2})$. When substituting in the diffraction integral and discretising the integration, the following is obtained:

$$\vec{E}(n,\theta) = C' \sum_{p=1}^{P-1}\left(\frac{\partial H_y}{\partial t}(p,n')\begin{pmatrix}\sin\theta\cos\theta\\ 0\\ -(\cos\theta)^2\end{pmatrix} - \frac{1}{\mathrm{Z}_0}\frac{\partial E_z}{\partial t}(p,n')\begin{pmatrix}\sin\theta\\ 0\\ -\cos\theta\end{pmatrix}\right)$$

with $n' = n - \mathrm{round}\Big(p\frac{\Delta s \sin\theta}{\mathrm{c}}\Big) + \frac{1}{2}$, which is the retarded time-step. The field can then be *Fourier* transformed into the frequency domain $\vec{E}(\omega,\theta)$.

Solution of the diffraction integral over the closed field-sampling surface has been split in four components. Dividing the reciprocal space in four quadrants with respect to the orthogonal directions of the grid and the direction of propagation of the incident field, for each angle of scattering in any quadrant the field is the resultant of the contributions of two sampling windows. For the diffraction in one quadrant, the addition of the far-field power densities from the two relevant windows gives the following electric field magnitude in far-field:

$$E(\omega, \theta) = \sqrt{E_1^2(\omega, \theta) \cos\theta + E_2^2(\omega, -90^\circ + \theta) \cos(-90^\circ + \theta)}, \tag{2.6}$$

where $E_1(\omega, \theta)$ and $E_2(\omega, -90^\circ + \theta)$ are the field contributions from two perpendicular windows at an angle θ with respect to the normal to the first sampling window. Although integration over the closed surface has been split into straight segments, with this method for any specific direction of propagation any signal sampled by different windows will have its spectra added constructively without the need to care for phase delays.

Finally, absolute values for the field intensities are obtained by normalisation of the power densities by the sum of all the power scattered in the completely computed cycle of directions.

2.4 Conclusion

The theoretical foundations for the present study of the optical diffraction of PCs have been presented in this chapter.

The laws governing the propagation of electromagnetic fields in linear and periodic dielectric media have been discussed in general, with details regarding the continuity of the fields, their projection on a basis of periodic functions, and the coupling between the resulting sets of linear equations.

Using the PWM and a purposely developed iterative band solver algorithm, an original investigation of the photonic band structure was carried out on rectangular and centred rectangular lattices. It was shown that for equivalent sets of geometrical parameters both lattices present bandgaps at the far side of the first *Brillouin* zone overlapping the visible range of wavelengths. The long-wavelength edges of the bandgaps are flat, *i.e.* they do not change with varying tangential component of the wave vector, and are shifted with changing polarisation and lattice. The results of the investigation on the rectangular lattice also showed that for propagation wave vectors within the edges of the *Brillouin* zone, gaps of up to 1% in relative width form on bands as low as the third one and cause these bands to be piecewise continuous.

For the sake of computing the diffraction efficiencies of periodic structures different methods must however be applied. Theoretical aspects of the diffraction of electromagnetic fields were introduced and field transformations were formalized for use in numerical computations presented later in this report. A system of two computational tools was presented here, which permits to compute accurate spectra of the light scattered in any direction by any two-dimensional dielectric arrangement for all angles of incidence, and therefore to obtain diffraction efficiencies. This task is dealt with in two steps. First, an FDTD algorithm numerically solves *Maxwell*'s equations for set initial and boundary conditions. Then, an NFFFT routine extracts the scattered fields from the data sampled at a closed surface of points during the first step. All the theoretical grounds and the numerical issues related to using this method for the purposes presented in the following chapters have been treated.